Article

TiN-NbN-TiN and Permalloy Nanostructures for Applications in Transmission Electron Microscopy

Michael I. Faley [1,2,*]🅳, **Joshua Williams** [1,2,3]🅳, **Penghan Lu** [1,2] **and Rafal E. Dunin-Borkowski** [1,2]🅳

1   Peter Grünberg Institute 5, Forschungszentrum Jülich, 52425 Jülich, Germany
2   Ernst Ruska-Centre for Microscopy and Spectroscopy with Electrons, Forschungszentrum Jülich, 52425 Jülich, Germany
3   Faculty of Engineering, University of Duisburg-Essen, 47057 Duisburg, Germany
*   Correspondence: m.faley@fz-juelich.de

Abstract: We fabricated superconducting and ferromagnetic nanostructures, which are intended for applications in transmission electron microscopy (TEM), in a commercial sample holder that can be cooled using liquid helium. Nanoscale superconducting quantum-interference devices (nanoSQUIDs) with sub-100 nm nanobridge Josephson junctions (nJJs) were prepared at a distance of ~300 nm from the edges of a 2 mm × 2 mm × 0.05 mm substrate. Thin-film TiN-NbN-TiN heterostructures were used to optimize the superconducting parameters and enhance the oxidation and corrosion resistance of nJJs and nanoSQUIDs. Non-hysteretic $I(V)$ characteristics of nJJs, as well as peak-to-peak quantum oscillations in the $V(B)$ characteristics of the nanoSQUIDs with an amplitude of up to ~20 μV, were obtained at a temperature ~5 K, which is suitable for operation in TEM. Electron-beam lithography, high-selectivity reactive ion etching with pure SF_6 gas, and a naturally created undercut in the Si substrate were used to prepare nanoSQUIDs on a SiN membrane within ~500 nm from the edge of the substrate. Permalloy nanodots with diameters down to ~100 nm were prepared on SiN membranes using three nanofabrication methods. High-resolution TEM revealed that permalloy films on a SiN buffer have a polycrystalline structure with an average grain dimension of approximately 5 nm and a lattice constant of ~0.36 nm. The $M(H)$ dependences of the permalloy films were measured and revealed coercive fields of 2 and 10 G at 300 and 5 K, respectively. These technologies are promising for the fabrication of superconducting electronics based on nJJs and ferromagnetic nanostructures for operation in TEM.

Keywords: titanium nitride; niobium nitride; nanofabrication; heterostructures; nanobridge Josephson junction; nanoSQUID; permalloy; nanodot; SiN membrane; transmission electron microscopy

1. Introduction

One of the most powerful methods for studying the microstructure of superconductors, in order to understand their crystal structure, stoichiometry, thin-film growth, and the formation of defects and grains that affect their superconducting properties, is transmission electron microscopy (TEM). The characteristic scale of local changes in the superconducting wave function is coherence length, which is on the order of 1 nm in high-T_c superconductors and a few nm in the thin films of Nb and NbN, which are commonly used in superconducting electronics. A Rayleigh spatial resolution down to ~120 pm and measurements of atomic displacements with an accuracy of better than 5 pm have been demonstrated in studies of grain boundaries in the high-T_c superconductor $YBa_2Cu_3O_{7-\delta}$ using aberration-corrected high-resolution TEM (HRTEM) [1]. Using commercially available sample holders [2,3], cooling down to ~5 K with TEM is now possible, enabling more comprehensive investigations of samples in their superconducting state. Applications of thin-film superconducting components in TEM are also becoming more feasible. Superconducting nanobridge Josephson junctions (nJJs) and nanoscale superconducting

quantum-interference devices (nanoSQUIDs) are particularly interesting, as they can be used in applications that include dissipation-free current leads for the generation and detection of magnetic fields and for the local generation of Josephson radiation of high-frequency electromagnetic fields. A nanoSQUID is defined as a sub-micron-sized loop of superconducting material, which includes two or more nJJs that have dimensions of ~100 nm or less.

The long-term stability of nJJs and nanoSQUIDs is an important issue, which is related to the corrosion resistance of the constituent superconducting materials. Although Nb oxidizes rapidly up to ~10 nm from its surface, exactly such a thickness is optimal because the coherence length of Nb films is ~10 nm. Nb films react with water and oxygen in laboratory air, with oxygen penetrating along grain boundaries through entire films of columnar-grown polycrystalline Nb to produce Nb_2O_5 crystallites that can expand and crack Nb film and nJJs. Pb films are unstable to degradation during thermal cycling between room temperature and an operating temperature of 5 K, leading to the formation of bumps and cavities in the film that can also destroy nJJs. Films of the high-temperature superconductor $YBa_2Cu_3O_{7-x}$ can decompose in air with the formation of carbonates.

Different methods of film surface passivation are used with varying degrees of efficiency. Coating of Nb films by a protective layer of NbN significantly suppress their oxidation as NbN is resistant to O_2, H_2, CO_2, and air. A passivating Si protective layer can be used to improve heat dissipation and to protect against mechanical and electrical fragility of devices, preventing nJJs from being destroyed by electrostatic discharges. Devices made from $YBa_2Cu_3O_{7-x}$ films usually require vacuum-tight encapsulation or can be partially protected by epitaxial films of $SrTiO_3$.

Epitaxial films of TiN and NbN have excellent corrosion resistance, which contributes to the long-term stability of nJJs and nanoSQUIDs. Thin films of NbN have a relatively large energy gap of 2Δ ~5 meV and T_c values of up to ~16 K. NanoSQUIDs based on NbN films were realized in ref. [4] and ref. [5]. However, due to the very short coherence lengths ξ ~5 nm of NbN films, $I(V)$ characteristics of nanoSQUIDs were hysteretic at operating temperatures of 4.2 K [4] and 5 K [5]. The interference pattern $I(B)$ were measured by detection of the switching current I_c and had a zig-zag form that is typical for nanoSQUIDs with long ($l \gg \xi$) weak-link bridges [6]. Unlike NbN films, TiN films have only recently begun to be used to fabricate nJJs and nanoSQUIDs. Thanks to the large coherence length $\xi(0) > 100$ nm at 4.2 K of TiN films, non-hysteretic variable-thickness TiN nJJs have been realized using electron-beam lithography (EBL) and reactive ion etching. Multilayers NbN/TiN films have even better mechanical, anticorrosion, and superconducting properties than single-layer NbN and TiN films [7–9]. The proximity effect between NbN and TiN layers yields the optimization of the superconducting parameters of nJJs and nanoSQUIDs made from NbN-TiN heterostructures by varying the deposition parameters and relative thickness of the superconducting layers. Presence of a TiN layer can lower T_c and resistivity and increase mean coherence length of the heterostructure compared to a pure NbN layer.

Superconducting and ferromagnetic materials are classified as quantum materials because the phenomena of superconductivity and ferromagnetism cannot be explained in the framework of classical physics. Ferromagnetism is based on the exchange interaction, which is a quantum-mechanical consequence of the Pauli exclusion principle and favors parallel alignment of the spins of unpaired electrons of neighboring atoms. The absence or very low dissipation during the transfer of superconducting or spin currents is beneficial for the operation of superconducting and ferromagnetic circuits on electron-transparent membranes under ultrahigh-vacuum TEM conditions, where heat removal is limited.

In general, very few experiments on larger superconductors have been performed below the superconducting transition temperature T_c in TEM. A free-standing permalloy ring enclosed between two 250 nm thick superconducting Nb rings of diameter 10 μm that served as a superconducting shield was placed on a Cu mesh and used to demonstrate the Aharonov–Bohm effect [10]. Flux vortices were imaged in large (>10 μm) lamellae or flakes of type II superconductors Nb [11], $YBa_2Cu_3O_{7-d}$ (YBCO) [12], $Bi_2Sr_2CaCu_2O_{8-\delta}$

(BSCCO) [12,13], and MgB_2 [14]. To date, no superconducting nanostructures with sizes below 1 μm that are thin enough to be transparent to an electron beam have been demonstrated to function on SiN membranes in TEM below T_c.

In the present work, we outline methods to prepare samples for this new direction of experiments, which can be performed using TEM. Superconducting bow-tie Dayem-type nJJs and nanoSQUIDs, as well as permalloy nanodots for joint superconductor–ferromagnetic spin resonance experiments, were prepared on SiN membranes for future operations in a helium-cooled holder using TEM.

2. Materials and Methods

E-beam-transparent SiN membranes with thicknesses ranging from 15 nm to 200 nm are available commercially and are among the most commonly used support films for imaging nanoparticles in TEM [15]. We used them as substrates, onto which superconducting and ferromagnetic films were deposited and nanostructured. As a practical alternative, we used 200 μm thick Si substrates that were buffered on both sides by 40 nm thick SiN films using low-pressure chemical vapor deposition (LPCVD). In the latter case, the superconducting and ferromagnetic films were deposited and nanostructured under standard conditions on bulk substrates, followed by wet chemical etching of the Si substrate in 20% KOH from the back side of the substrate to the back side of the SiN buffer layer using commercial wafer holders [16]. Alternatively, and more commonly, home-made analogues for etching substrates with standard sizes of 10 mm × 10 mm × 0.3 mm or 20 mm × 20 mm × 0.3 mm are used. The measured etch rate of Si in a 20% solution of KOH in water was approximately 9 nm/h. This etch rate can be compared with the 6 μm/min etch rate of the Si substrate by reactive ion etching (RIE) enhanced by an inductively coupled plasma (ICP) and performed in pure SF_6 gas [17].

2.1. Superconducting Nanostructures

The substrates were cleaned in acetone, propanol, and deionized water and etched with an Ar+ ion beam just before placing them in a home-built sputtering machine, which was evacuated to a base pressure of <4×10^{-8} mbar using oil-free pumps. TiN and NbN films were deposited at a rate of ~3 nm/min from 50 mm 99.95% pure TiN and NbN targets using pulsed reactive DC magnetron sputtering. The substrates were lying freely on a heater. The heater temperature was 920 °C during TiN deposition and 800 °C during NbN deposition. Deposition was performed in an Ar(80%)-N_2(20%) gas mixture at a total pressure of 10^{-2} mbar. A N_2 flow of 5 mln/min was regulated using a Brooks© 5850 TR mass flow controller. Ar and N_2 gases had a purity of 99.9999% and contained less than 0.01 ppm O_2, which corresponds to an O_2 partial pressure of less than 10^{-10} mbar. Before deposition, the chamber was outgassed under deposition conditions during pre-sputtering onto the closed shutter for more than 1 h.

A thin-film TiN-NbN-TiN multilayer heterostructure was used for the preparation of superconducting nanowires, Dayem-type nJJs, and nanoSQUIDs. As shown in ref. [18] and ref. [19], TiN and NbN thin films exhibit good superconducting properties when they are deposited onto an LPCVD SiN buffer layer and grown epitaxially on top of each other. The lattice constants of TiN and NbN are 0.424 nm and 0.439 nm, respectively. The lowest 3 nm thick TiN layer served as a buffer layer for the subsequent NbN film and improved its T_c and critical current. The uppermost 15 nm thick TiN layer in the TiN-NbN-TiN heterostructure served for the fine setting of T_c and for the protection of the 15 nm thick NbN layer from corrosion and oxidation during patterning by EBL and subsequent resist removal using warm acetone.

The insertion of the superconducting NbN layer in between two TiN layers allows the T_c value of the heterostructure to be tuned for the improved operation of nJJs at the stabilized temperature of the TEM sample holder. This insertion also reduces the width of the superconducting transition in the $R(T)$ dependence. The latter behavior reflects a reduction in thermally activated flux motion and a higher critical current density in

such a heterostructure. Additional passivation by a thin Si layer can also improve the thermal sink and provide protection against the mechanical and electrical fragility of the devices. The $R(T)$ dependence of the TiN(3 nm)-NbN(15 nm)-TiN(15 nm)-Si(330 nm) heterostructure measured using Quantum Design (QD) Physical Property Measurement Systems (PPMS) is shown in Figure 1a. The heterostructure has $T_c \cong 7.5$ K, while the superconducting transition temperatures of TiN and NbN films of thicknesses >200 nm deposited under similar conditions were 5 and 16 K, respectively. The $T_c \cong 7.5$ K value for the heterostructure is smaller than the T_c value for NbN films of similar thickness due to the proximity effect with the covering TiN film, but it is optimal for non-hysteretic operation of nJJs and nanoSQUID at the operating temperature of 5 K, which can be realized in a TEM sample holder.
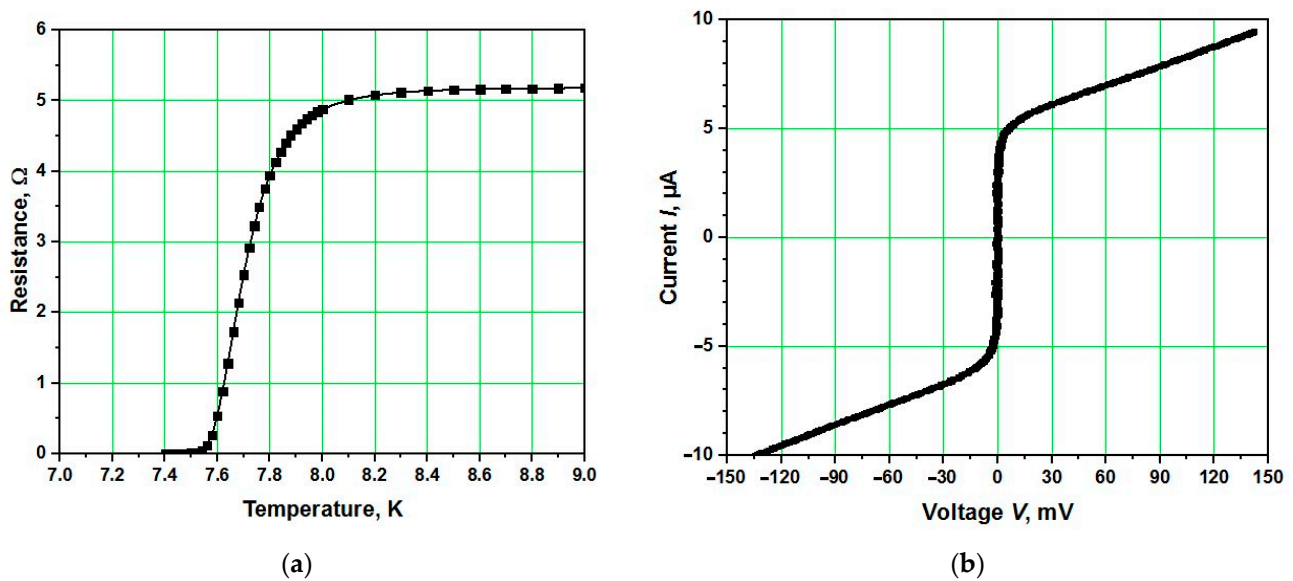

(a)   (b)

Figure 1. (**a**) $R(T)$ dependence of the TiN(3 nm)-NbN(15 nm)-TiN(15 nm)-Si(330 nm) heterostructure. (**b**) Hysteresis-free $I(V)$ dependence measured from a 30 nm wide TiN-NbN-TiN nJJ at 5 K.

Figure 1b shows non-hysteretic $I(V)$ dependence measured for a 30 nm wide TiN-NbN-TiN nJJ at 5 K. Non-hysteretic $I(V)$ characteristics of nJJs are required for the use of conventional readout techniques to operate nanoSQUIDs as magnetic flux-to-voltage converters. The critical current $I_c \cong 5$ μA and the normal state resistance $R_n \cong 30$ Ω correspond to current density in the Nb layer of $J_c \cong 1$ MA/cm^2 and a characteristic voltage of the nJJ of $V_c = I_c R_n \cong 150$ μV. A nanoSQUID with such nJJs demonstrates peak-to-peak quantum oscillations in its $V(B)$ characteristics with an amplitude of up to ~20 μV, as shown in Figure 2.

The Ginzburg–Landau coherence length $\xi(T) \propto \left(1 - \frac{T}{T_c}\right)^{-1/2}$ is the characteristic scale over which spatial variations in the superconducting order parameter occur. Constriction of a size smaller than the "critical" length, i.e., $L_c = 3.49\xi$, patterned in a superconducting film behaves as Josephson junctions [6,20]. By measuring the resistance of the TiN-NbN-TiN heterostructure as a function of the magnetic field using the QD PPMS at 4.2 K, we determined a critical magnetic field of $B_{c2} \cong 7$ T and the superconducting coherence length $\xi(4.2 \text{ K}) \cong \sqrt{\Phi_0/2\pi B_{C2}} \cong 6$ nm. This coherence length corresponds to $L_c \cong 30$ nm at 6 K, which in turn corresponds to the current thickness of the TiN-NbN-TiN heterostructure and the typical width and length of nJJs that we can achieve using EBL. The coherence length in the TiN-NbN-TiN heterostructure is slightly larger than that in NbN films of a similar thickness due to the proximity effect of the TiN film.
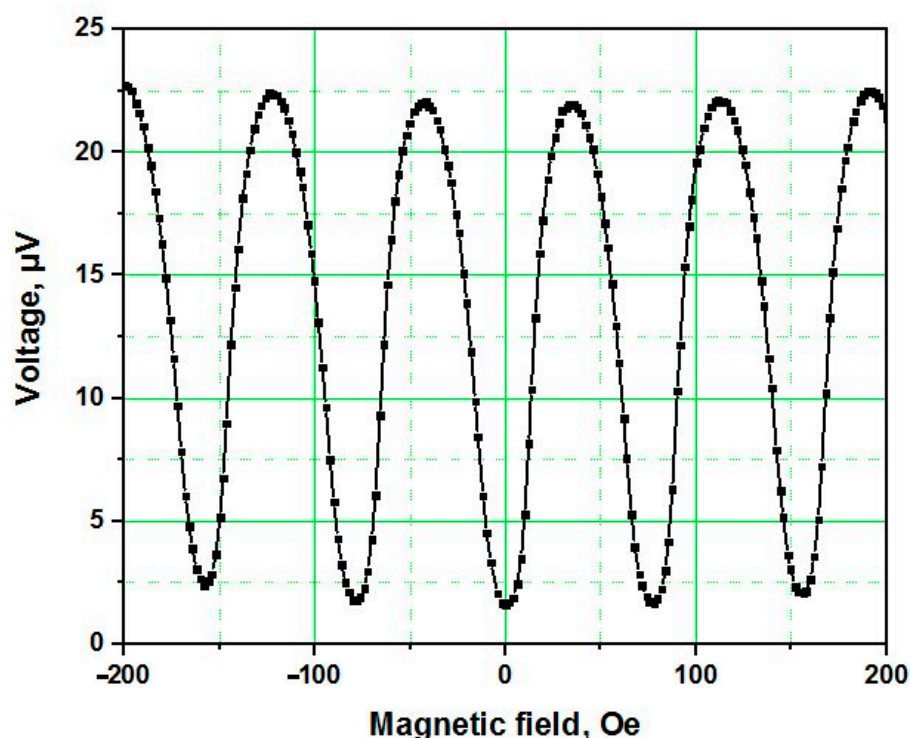
Figure 2. *V*(*B*)–characteristic of a planar nanoSQUID with TiN-NbN-TiN nJJs measured using a QD PPMS with a bias current of 12 μA at 5 K.

Patterning of the 30 nm thick TiN-NbN-TiN heterostructures was performed using highly selective RIE with pure SF_6 gas and 100 nm thick masks of AZ nLof2020 resist, diluted by AZ EBR thinner with a ratio of 1:3. When compared with masks of diluted HSQ resist [21], diluted nLof2020 resist has the advantages of requiring a ~10 times lower dose of electron-beam exposure and its residuals after RIE can be removed by easily using warm acetone. A passivating Si layer was deposited after removal of the resist residuals for improved coverage of the completed patterned structures. The use of pure SF6 gas in RIE provides several benefits when compared to physical etching using an Ar+ ion beam, including ~3 times faster etch rates for TiN and NbN in comparison to SiN and the diluted nLof2020 resist, no formation of fences due to redeposition, and a slight undercut. The 30 nm thick TiN-NbN-TiN heterostructures have an undercut of ~10 nm, which is ~3 times smaller than the undercut observed in the preparation of pure 100 nm thick TiN nJJs [22]. The smaller undercut resulted in improved reproducibility of the nJJs and a spatial resolution of the superconducting nanostructures that approached the spatial resolution of the mask of the electron-beam resist.

EBL, high-selectivity RIE with pure SF_6 gas, and a naturally created undercut in the Si substrate were used to prepare nanoSQUIDs on a SiN membrane within ~500 nm of the edge of the substrate, similar to the results demonstrated in [17] on a 10 nm thick SiO_2 membrane (see Figure 3a). Another potential option is to place a nanoSQUID near the corner or edge of a small substrate and integrate it in a TEM sample holder. Figure 3b shows an SEM image of a planar nanoSQUID with nJJs structured using RIE, placed at a distance of ~300 nm from the edges of a 2 mm × 2 mm × 0.05 mm substrate using focused ion beam (FIB) nanosculpturing and an Al sacrificial layer. The object under study can be placed near the nanoSQUID, for example, on an electron-beam-transparent membrane or TEM grid in a flip-chip configuration. Such a configuration has the advantage of better heat removal from the nJJs and nanoSQUID during their operation in a finite-voltage state. The achieved 300 nm separation of planar nanoSQUIDs from the substrate corner can be compared with the state-of-the-art approximately 10 μm distance that was demonstrated in [23].
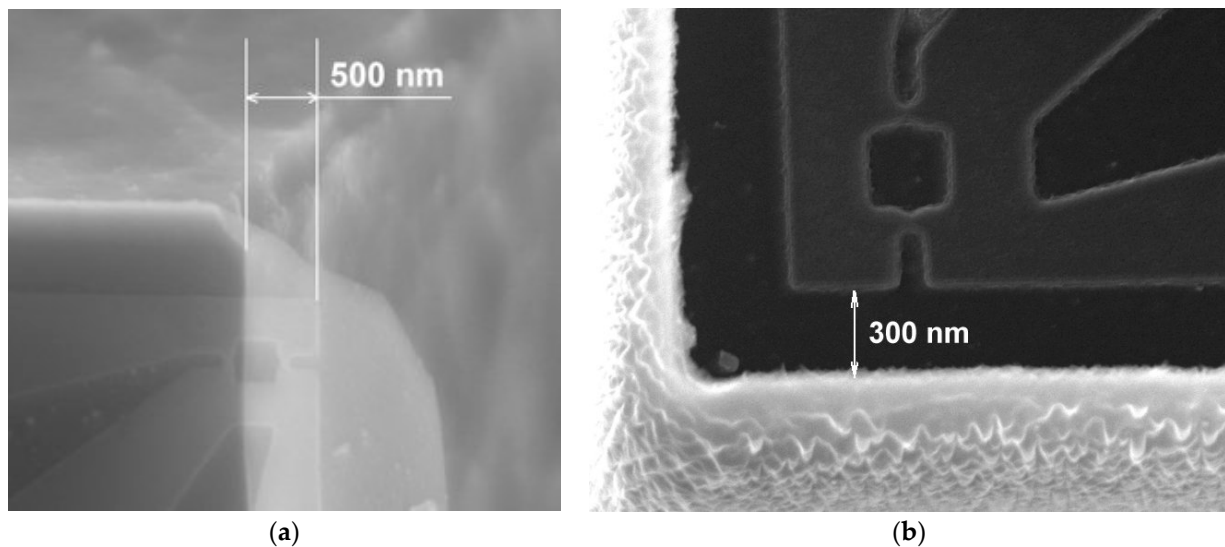
(a)   **(b)**

Figure 3. (**a**) SEM image of a nanoSQUID placed within a distance of 500 nm from the corner of a Si cantilever chip on a 10 nm thick SiO_2 membrane. (**b**) SEM image of a planar nanoSQUID with nJJs structured using RIE, placed at a distance of ~300 nm from the edges of a 2 mm $\times$ 2 mm $\times$ 0.05 mm substrate using FIB nanosculpturing and an Al sacrificial layer.

If heat removal from the operating nJJs and nanoSQUID is insufficient, then thermal hysteresis of the $I(V)$ characteristics occurs. Thermal hysteresis is a result of overheating of the nJJ when its superconducting current exceeds the critical current. The dissipated energy then heats the nJJ above T_c, so that the nanobridge enters the normal conducting state [24]. As a result of Joule heat dissipated on the normal conducting nanobridge, its temperature also rises, which in turn reduces the retrapping critical current I_r. The ratio of I_c to I_r depends on thermal coupling between the nJJ and the substrate and is greater in the case of poor heat removal (for example, in the case of free-standing nJJs or nJJs on membranes). Pure thermal hysteresis occurs when the bias current is close to the depairing current of the superconducting film, which is typically higher than the combined critical currents of the nJJs in the nanoSQUID. However, this effect cannot be used to measure magnetic fields because it does not depend on magnetic flux through the loop of the nanoSQUID [18].

Other nanofabrication methods, which are described in the next section, are currently also used for the preparation of nanostructures of other superconducting materials, such as Al and YBCO, which cannot be structured by RIE on bulk substrates. It is possible that in the future, these methods will also be used for the preparation of superconducting nanostructures on membranes for applications in TEM. In the case of YBCO, the membrane can be made from, for example, $SrTiO_3$ (STO); epitaxial growth of STO on Si and its use as a buffer layer have been demonstrated in [25]. High-quality YBCO films can be grown on STO buffer layers and should not be too thick to be electron-beam-transparent in TEM, as well as to avoid cracks due to the different thermal expansion coefficients of YBCO and Si.

2.2. Permalloy Nanostructures

Permalloy is a Ni-Fe alloy that contains ~80% Ni and ~20% Fe and is compatible with CMOS applications [26], making it a preferred choice for ferromagnetic materials in electronics. In addition, permalloy is a soft magnetic material with small coercivity [27], high permeability, and high saturation magnetization [28]. We deposited thin films of permalloy at room temperature using dc magnetron sputtering from a single target in a pure Ar atmosphere at a pressure of ~1 Pa. The permalloy target had a diameter of 35 mm, but the intense plasma was only produced in an area of diameter ~8 mm using a special arrangement of a wide-ring magnet and a small-diameter Fe guide for the magnetic flux, as shown in Figure 4a. For a target–substrate distance of ~8 cm, the sputtered material approaches the substrate almost as a parallel beam, which is advantageous for the use of

shadow/stencil masks for the fabrication of permalloy nanostructures. Figure 4b shows $M(H)$ dependences measured from a 5 mm × 4 mm × 40 nm permalloy film deposited using this method, revealing coercive fields of 2 and 22 G at temperatures of 300 and 5 K, respectively.

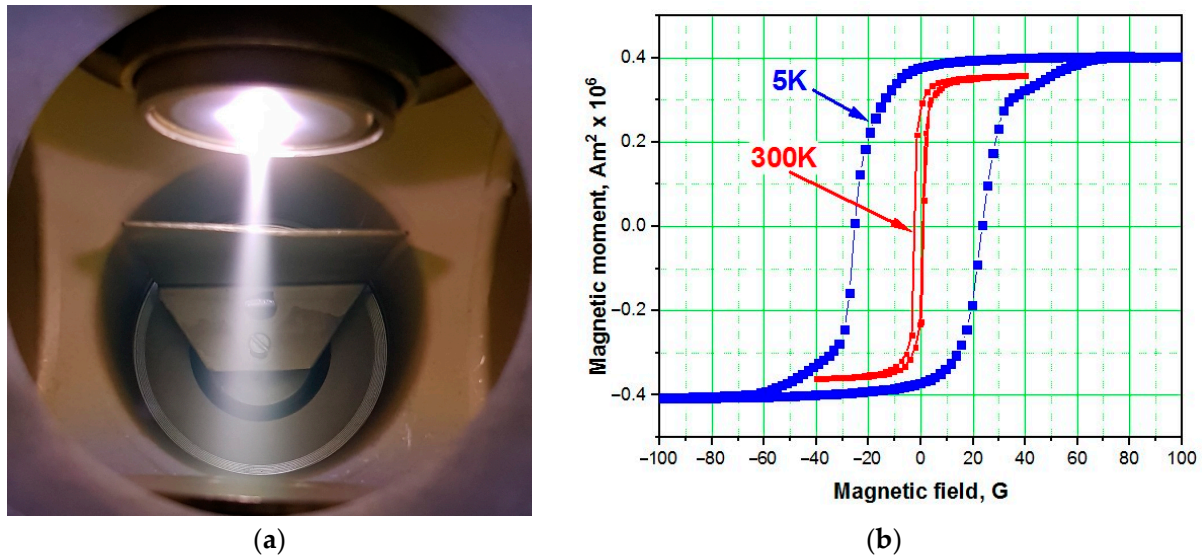(**a**)　　　　　　　　　　　　　　　　　　　　　(**b**)

Figure 4. (**a**) DC magnetron sputtering of permalloy. The target–substrate distance is ~8 cm. (**b**) $M(H)$ dependences measured from a 5 mm × 4 mm × 40 nm permalloy film deposited using this method, revealing coercive fields of 2 and 22 G at 300 and 5 K, respectively.

In principle, permalloy thin films can be nanostructured using RIE enhanced by an inductively coupled plasma (ICP) [29]. However, due to possible contamination of the available RIE machine, this method of patterning is undesirable. Instead of RIE, we prepared permalloy nanostructures using three different fabrication methods that were adapted for deposition on 40 nm thick SiN membranes: (1) lift-off; (2) ion beam etching (IBE); and (3) stencil lithography. These methods and the obtained results are described in the following three subsections.

2.2.1. Lift-Off

We used a bilayer of PMMA positive electron-beam resist to create an undercut structure, which ensures a clean lift-off process. The lower copolymer PMMA AR-P 617-08 (33%) layer has thickness of ~400 nm and required an electron-beam exposure dose of 180 μC/cm². The upper resist PPMA AR-P 679.04 (950 K) layer had a thickness of ~300 nm and required an e-beam exposure dose of 600 μC/cm². A nominal diameter of up to 1 μm was exposed with the highest dose, while a lower dose was used for additional-offset electron-beam exposure of the pattern to achieve a larger undercut, as shown in Figure 5a. In both cases, the accelerating voltage of the electron beam was 100 kV, which provided penetration of the electron beam through the entire 0.7 μm thickness of the bilayer resist and its homogeneous exposure.

After 15 min of development of the bilayer PMMA resist in the AR 600-56 (MIBK) developer, an undercut that was up to 2 μm deep was achieved, as shown in Figure 5b. The result of the offset exposure and long development time was controlled by observing a cross-section of the bilayer resist mask using scanning electron microscopy (SEM) in snapshot mode to avoid the flow and fall of the overhanging areas of the resist mask. This approach resulted in a reduced quality of the SEM image. Similar masks with a large undercut and a lift-off method can be used for double-angle shadow evaporation of Al for the in situ preparation of three-layer Al tunnel junctions for quantum bits.
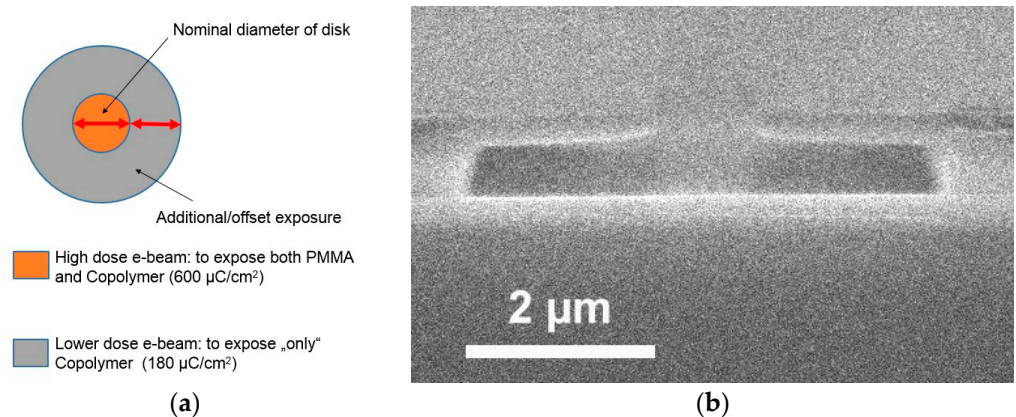
(**a**)   (**b**)

Figure 5. (**a**) Schematic diagram of the double exposure method for the creation of a large undercut in a bilayer of PMMA resist. (**b**) SEM image of a cross-section of the patterned bilayer resist containing a 2 μm undercut and a hole for the preparation of a permalloy disk of nominal diameter ~900 nm.

Flow of the PMMA resist mask occurs at a relatively low temperature of approximately 120 °C. This temperature can be reached unintentionally in the case of insufficient heat removal from the sample during deposition of the permalloy film. Apiezon® vacuum grease was used for thermal contact between the back side of the substrate and a massive metal plate that served as a sample holder. After deposition of the permalloy film, residuals of the Apiezon® vacuum grease were removed using Limonene solvent and the lift-off process was performed in acetone at 70 °C. The SEM and TEM images of the resulting permalloy nanodots are shown in Figure 6.

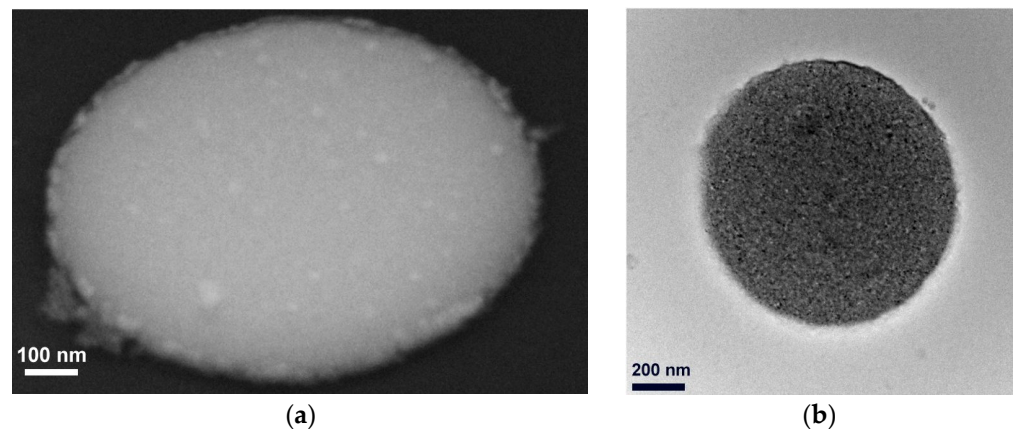(**a**)   (**b**)

Figure 6. (**a**) SEM image of a permalloy nanodisk with a diameter of ~1 μm fabricated using lift-off with a mask of bilayer resist. The image was recorded at a 45° sample tilt angle. (**b**) TEM image of a 60 nm thick permalloy nanodisk with a diameter of ~900 nm manufactured using lift-off with a bilayer resist.

During lift-off, the metal on the resist was washed off by placing the sample in acetone while the desired pattern remained attached to the substrate where there is a resist opening. As a result of the large undercut, the lift-off process takes place with almost no debris at the edges of the nanodots, in contrast to the case where a single-layer positive resist mask is used. Smooth edges of the nanodots are preferred because their coercivity increases with edge roughness [30]. Several holes in the upper layer of the bilayer resist mask can share the same opening in the lower layer, allowing dense arrays of permalloy nanodots to be produced, as shown in Figure 7a.
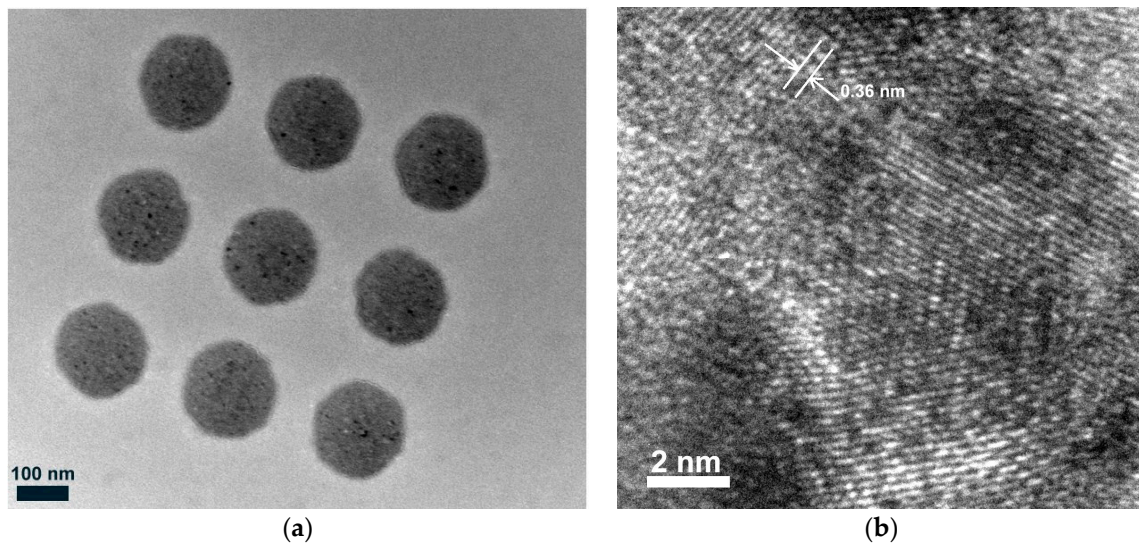
Figure 7. (**a**) TEM image of an array of 60 nm thick permalloy nanodisks with diameters of ~200 nm manufactured by EBL with lift-off using a bilayer resist. (**b**) High-resolution TEM image of a small part of one of the permalloy nanodisks.

High-resolution TEM images of permalloy nanodisks revealed polycrystalline films with arbitrary grain orientations, an average grain size of ~5 nm, and a lattice constant of ~0.36 nm, as shown in Figure 7b.

Figure 8 shows an SEM image of a 50 nm thick SiN membrane with a 300 nm permalloy nanodisk. The membrane area is darker in the SEM image.

Figure 8. SEM image of a 50 nm thick SiN membrane with a 300 nm permalloy nanodisk.

2.2.2. Ion Beam Etching

IBE is a dry physical etching technique, which potentially provides a better spatial resolution than the lift-off method described above. A 200 nm thick mask from negative AZ nLof2020 resist diluted with AZ EBR solvent in a 1:2 ratio was used for the preparation of permalloy nanodisks on membranes. An Ar$^+$ ion beam at normal incidence to the substrate surface was used to etch 100 nm thick permalloy films, while an electron-beam-patterned negative resist mask preserved the desired structure. The substrate was clamped to a water-cooled, rotating metal plate. Redeposited material created fences at the edges of the structures, which could affect the magnetic properties of the nanodisks and were removed using an additional IBE step performed at a grazing angle of ~5° after removal of the residual resist using warm acetone. In order to minimize membrane etching, the etching time was chosen so that, after IBE first performed in a direction perpendicular to the substrate surface, a few nm thick permalloy film still remained on the open surface areas, which was then removed during a second IBE step at a grazing angle.

Figure 9 shows images of 100 nm thick permalloy disks made by IBE: (a) SEM image of a disk with a diameter of 900 nm; and (b) a TEM image of a disk with a diameter of 500 nm. It was observed that IBE resulted in better reproducibility of cylinder-shaped disks, with an absence of half shadow edge smoothing and debris (Figure 9a), but led to inhomogeneous etching of the membrane. After IBE, the opened membrane areas demonstrated increased roughness and remained thicker near the nanodots due to the reduced etch rate near the structures and the redeposition of the permalloy (see Figure 9b). The significantly thinner membrane away from the nanostructures can weaken the total mechanical stability of the entire membrane.

(a)   **(b)**
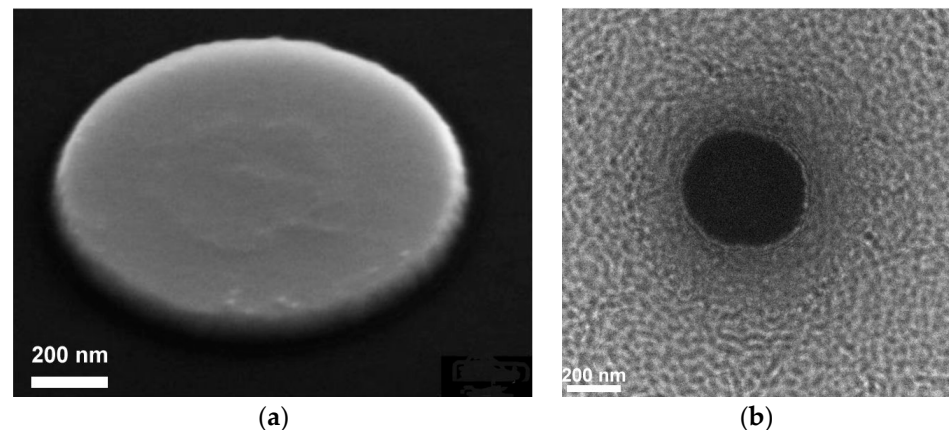
Figure 9. Permalloy nanodisks with a thickness of 100 nm made by IBE: (**a**) SEM image of a nanodisk with a diameter of 900 nm and (**b**) TEM image of a nanodisk with a diameter of 500 nm. The SEM image was recorded at a 45° sample tilt angle.

The formation of fences during IBE was reduced using a reflowed resist mask by heating it above the resist softening point. For this purpose, the samples were kept with the resist mask on a heater plate for 5 min at 150 °C before etching, as shown in Figure 10a–d. This process changed the shape of the top surface of the resist as a result of surface tension, similarly to the meniscus of a drop of water, while maintaining the diameter of the disk near the substrate surface. Due to the tilted resist surface at the edges, there was much less redeposited material on it, and it was partially removed during IBE. Although some residue was still present after IBE when using such a reflow resist mask, this was found to be useful for minimizing redeposition and creating much shorter fences, thereby reducing the time required for additional etching and maintaining the mechanical stability of the free-standing membrane.

Arrays of nanodots were produced using IBE, as shown in Figure 11. The reduced etch rate near each nanodot in the array led to a further reduction in the thickness of the membrane far from the array. Mutual shadowing of the fences also interfered with their removal using IBE at a grazing angle.

In general, when compared with lift-off, IBE resulted in cleaner and more controllable/reproducible structures with better spatial resolution, especially in the case of etching of much thinner films, which allowed for a much thinner resist to be used. However, the reduced thickness of the membrane away from the structures after IBE can degrade its mechanical stability.

2.2.3. Stencil Lithography

Ideally, the nanostructures should be deposited directly on an extremely thin membrane, such as 1-atom-thick graphene, without being affected by wet lithography or dry etching that can contaminate and degrade the surfaces and destroy the membrane. The use of shadow masks (stencils) can potentially solve this problem if sufficient spatial resolution is provided. Stencil lithography has been developed widely in recent years and has been used to achieve sub μm sized apertures and structures [31–34]. It is based on

stencils with nanometer-sized apertures milled into a SiN membrane using, for example, FIB milling. The membrane can be identical to the membrane, on to which the films should be deposited. This method is compelling, not only because it avoids the use of EBL and any related chemical and etching processes, but also because the mask is reusable.
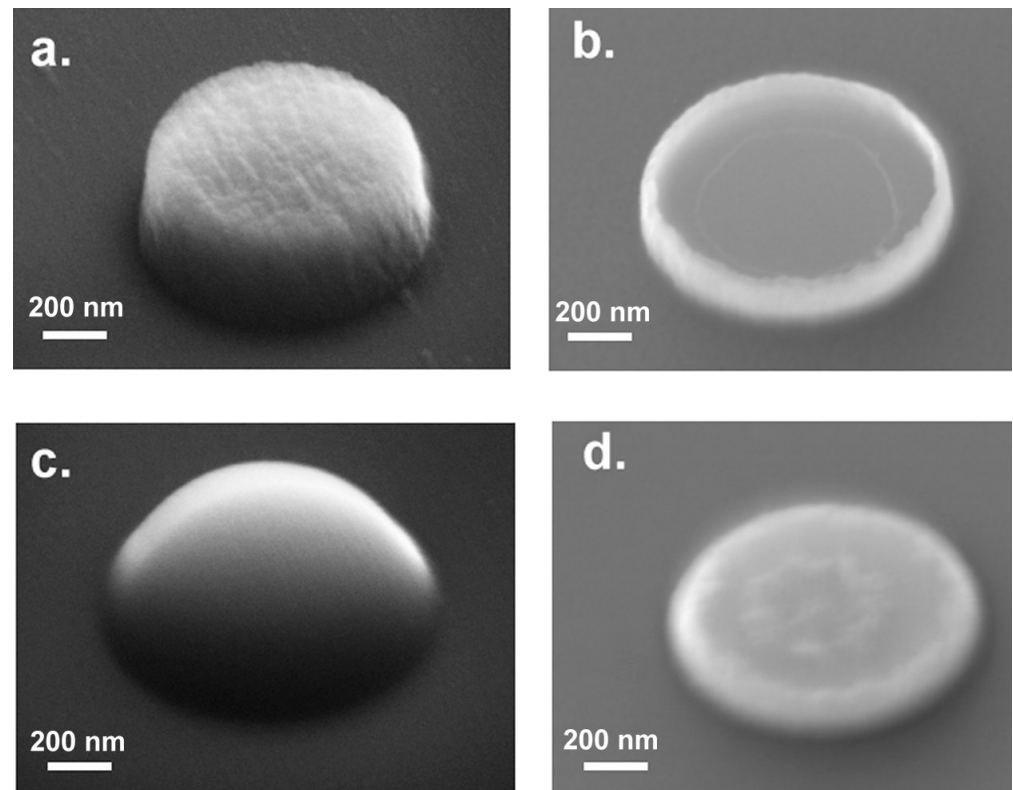

Figure 10. (**a**) SEM image of a developed resist structure with a diameter of 900 nm; (**b**) SEM image of a permalloy nanodisk after IBE made using the resist mask shown in Figure 10a; (**c**) SEM image of a melted resist structure with a diameter of 1 μm; (**d**) SEM image of a permalloy nanodisk after IBE made from the resist mask shown in Figure 10c. The images were recorded at a 45° sample tilt angle.
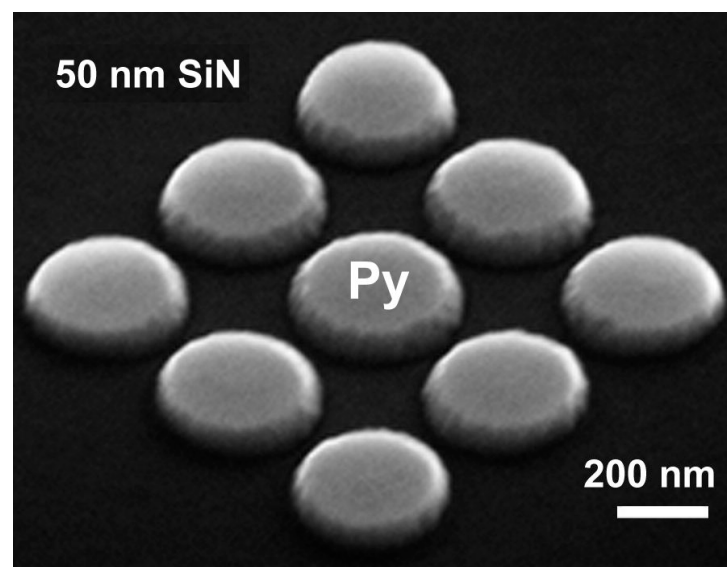
Figure 11. SEM image of an array of 50 nm thick permalloy nanodisks with diameters of ~300 nm made using EBL and IBE. The image was recorded at a 45° sample tilt angle.

We prepared shadow masks based on 40 nm thick SiN membranes. Prior to milling holes using FIB milling, each membrane was covered by a 500 nm thick layer of Al for protection from undesired etching during secondary electron imaging with excitation by Ga$^+$ ions, as well as stigmatism and focus alignment of the ion beam before milling. The stencil and sample were aligned and fixed in a flip-chip configuration under an optical microscope in transient illumination. Spacers that were 500 nm thick were made on the stencil from an Al film beyond the membrane area and separated from the sample. The resulting stencil and permalloy nanodisks deposited through the mask are shown in Figure 12a,b, respectively.
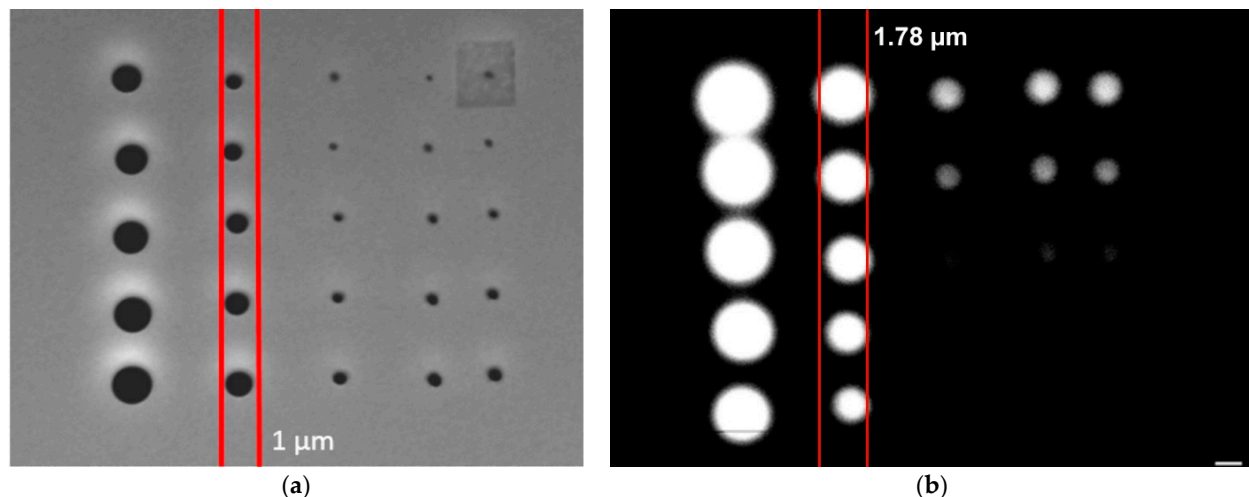
Figure 12. (**a**) SEM image of shadow masks, showing an Al-coated SiN membrane on a TEM grid for TEM with holes created using FIB milling. (**b**) SEM image of permalloy nanodisks deposited through the perforated SiN membrane shown in (**a**), which was used as a stencil.

The spatial resolution achieved using our home-made stencils was ~200 nm and was limited primarily by the stencil–sample separation, which included not only the thickness of the Al spacers but also bending of the perforated membrane and possible contamination of the surfaces by sub µm sized debris. Further optimization of the preparation of the stencil mask and the alignment of the stencil and sample in clean-room conditions promise to provide a controllable separation between the stencil and sample and to significantly improve the spatial resolution and reproducibility of this method in the future.

3. Conclusions

We compared different methods for the nanofabrication of TiN-NbN-TiN nJJs and nanoSQUIDs and permalloy nanodisks on membranes for applications in TEM. Such nanostructures are intended for applications using a commercial TEM sample holder that can be cooled using liquid He. This work is motivated by the development of improved cryogenically cooled TEM sample holders that yield measurements at temperatures down to ~5 K, as well as by the development of Lorentz, holographic, differential phase contrast, and ptychographic TEM techniques that allow for the study of magnetic domains in ferromagnetic nanostructures. The combined operation of superconducting and ferromagnetic nanostructures in TEM is conceivable. Low-energy dissipation in such superconducting and spintronic devices is essential because heat removal from membranes in TEM is challenging.

The use of TiN-NbN-TiN heterostructures helps to optimize the superconducting parameters of nitride superconductors for the desired operating temperature of ~5 K and enhances the corrosion resistance of the nJJs and nanoSQUIDs. Additional passivation by an amorphous Si layer improves heat removal from the nJJs and nanoSQUIDs in the finite-voltage state and protects them from mechanical and electrical fragility. The high selectivity

of RIE of the nitride superconductors relative to the resist, SiN, and SiO_2 membranes allows for the fabrication of sub-100 nm wide TiN-NbN-TiN Dayem-type nJJs on membranes. Nanosculpturing of substrates using FIB allows nanoSQUID to be placed only ~300 nm from the substrate edges, making it possible to realize a short distance from objects under study in a flip-chip configuration with standard TEM grids.

Various methods, including lift-off, IBE, and stencil lithography, were tested and compared for the nanopatterning of permalloy films. They each allow the fabrication of permalloy nanodots on SiN membranes and have their own advantages and disadvantages. A surprisingly large (up to 2 μm) undercut in a bilayer resist allows for gentle lift-off preparation of nanodisks on SiN membranes. This method seems to be the most suitable at present. However, in some cases, after further optimization and application of appropriate precautions, it can be replaced by RIE, IBE, or stencil lithography.

4. Summary

Four methods for the fabrication of superconducting and permalloy nanostructures on membranes are compared. NanoSQUIDs with sub-100 nm nanobridge Josephson junctions (nJJs) were prepared at a distance of ~300 nm from the edges of a 2 mm × 2 mm × 0.05 mm substrate. Ultrathin TiN-NbN-TiN heterostructures were used to optimize the superconducting parameters and to enhance the oxidation and corrosion resistances of the nJJs and nanoSQUIDs. Our measurements revealed non-hysteretic $I(V)$ characteristics of nJJs and nanoSQUIDs, as well as peak-to-peak quantum oscillations in the $V(B)$ characteristics of nanoSQUIDs with an amplitude of up to ~20 μV. Electron-beam lithography, high-selectivity reactive ion etching with pure SF_6 gas, and a naturally created undercut in the Si substrate were used to prepare nanoSQUIDs on SiN membranes within ~500 nm from the substrate edges. Permalloy nanodots with diameters down to ~100 nm were prepared on SiN membranes using three nanofabrication methods: lift-off, ion beam etching, and stencil lithography. The demonstrated techniques are promising for the fabrication of superconducting electronics based on nJJs and permalloy nanostructures for combined operation on membranes at cryogenic temperatures using TEM.

References

1. Houben, L.; Thust, A.; Urban, K. Atomic-precision determination of the reconstruction of a 90° tilt boundary in YBa₂Cu₃O₇₋ by aberration corrected HRTEM. *Ultramicroscopy* **2006**, *106*, 200–214. [CrossRef]
2. Available online: https://condenzero.com/ (accessed on 30 April 2023).
3. Available online: https://www.gatan.com/products/tem-specimen-holders/cooling-situ-holders (accessed on 30 April 2023).
4. Russo, R.; Esposito, E.; Crescitelli, A.; Di Gennaro, E.; Granata, C.; Vettoliere, A.; Cristiano, R.; Lisitskiy, M. NanoSQUIDs based on niobium nitride films *Supercond. Sci. Technol.* **2017**, *30*, 024009.
5. Holzman, I.; Ivry, Y.; Holzman, I.; Ivry, Y. On-chip integrable planar NbN nanoSQUID with broad temperature and magnetic-field operation range. *AIP Adv.* **2019**, *9*, 105028. [CrossRef]

6. Likharev, K. Superconducting weak links. *Rev. Mod. Phys.* **1979**, *51*, 101–159. [CrossRef]
7. Sugumaran, A.A.; Purandare, Y.; Shukla, K.; Khan, I.; Ehiasarian, A.; Hovsepian, P. TiN/NbN Nanoscale Multilayer Coatings Deposited by High Power Impulse Magnetron Sputtering to Protect Medical-Grade CoCrMo Alloys. *Coatings* **2021**, *11*, 867. [CrossRef]
8. Barshilia, H.C.; Prakash, M.S.; Poojari, A.; Rajam, K.S. Corrosion behavior of nanolayered TiN/NbN multilayer coatings prepared by reactive direct current magnetron sputtering process. *Thin Solid Film.* **2004**, *460*, 133. [CrossRef]
9. Zhang, J.J.; Su, X.; Zhang, L.; Zheng, L.; Wang, X.F.; You, L. Improvement of the superconducting properties of NbN thin film on single-crystal silicon substrate by using a TiN buffer layer. *Supercond. Sci. Technol.* **2013**, *26*, 045010. [CrossRef]
10. Tonomura, A.; Osakabe, N.; Tsuyoshi, T.; Kawasaki, T.; Endo, J.; Yano, S.; Yamada, H. Evidence for Aharonov-Bohm Effect with Magnetic Field Completely Shielded from Electron wave. *Phys. Rev. Lett.* **1986**, *56*, 792–795. [CrossRef]
11. Harada, K.; Matsuda, T.; Bonevich, J.; Igarashi, M.; Kondo, S.; Pozzi, G.; Kawabet, U.; Tonomura, A. Real-time observation of vortex lattices in a superconductor by electron microscopy. *Nature* **1992**, *360*, 51–53. [CrossRef]
12. Tonomura, A.; Kasai, H.; Kamimura, O.; Matsuda, T.; Harada, K.; Yoshida, T.; Akashi, T.; Shimoyama, J.; Kishio, K.; Hanaguri, T.; et al. Observation of Structures of Chain Vortices inside Anisotropic High-T_c Superconductors. *Phys. Rev. Lett.* **2002**, *88*, 237001. [CrossRef] [PubMed]
13. Loudon, J.C.; Midgley, P.A. Imaging flux vortices in type II superconductors with a commercial transmission electron microscope. *Ultramicroscopy* **2009**, *109*, 700–729. [CrossRef]
14. Cottet, M.J.G.; Cantoni, M.; Mansart, B.; Alexander, D.T.L.; Hébert, C.; Zhigadlo, N.D.; Karpinski, J.; Carbone, F. Quantitative imaging of flux vortices in the type-II superconductor MgB2 using cryo-Lorentz transmission electron microscopy. *Phys. Rev. B* **2013**, *88*, 014505. [CrossRef]
15. Available online: https://www.tedpella.com/grids_html/silicon-nitride.aspx (accessed on 30 April 2023).
16. Available online: https://www.ammt.com/products/wet-etching/single-series/ (accessed on 30 April 2023).
17. Faley, M.I.; Bikulov, T.; Bosboom, V.; Golubov, A.A.; Dunin-Borkowski, R.E. Bulk nanomachining of cantilevers with Nb nanoSQUIDs based on nanobridge Josephson junctions. *Supercond. Sci. Technol.* **2021**, *34*, 035014. [CrossRef]
18. Faley, M.I.; Fiadziushkin, H.; Frohn, B.; Schüffelgen, P.; Dunin-Borkowski, R.E. TiN nanobridge Josephson junctions and nanoSQUIDs on SiN-buffered Si. *Supercond. Sci. Technol.* **2022**, *35*, 065001. [CrossRef]
19. Faley, M.I.; Dunin-Borkowski, R.E. A Self-Flux-Biased NanoSQUID with Four NbN-TiN-NbN Nanobridge Josephson Junctions. *Electronics* **2022**, *11*, 1704. [CrossRef]
20. Aslamazov, L.G.; Larkin, A.I. Josephson effect in superconducting point contacts. *Pisma Zh. Eksp. Teor. Fiz.* **1968**, *9*, 150–154.
21. Rodrigo, R.; Faley, M.I.; Dunin-Borkowski, R.E. NanoSQUIDs based on Nb nanobridges. *J. Phys. Conf. Ser.* **2020**, *1559*, 012011. [CrossRef]
22. Faley, M.I.; Liu, Y.; Dunin-Borkowski, R.E. Titanium nitride as a new prospective material for nanoSQUIDs and superconducting nanobridge electronics. *Nanomaterials* **2021**, *11*, 466. [CrossRef]
23. Hasselbach, K.; Ladam, C.; Dolocan, V.O.; Hykel, D.; Crozes, T.; Schuster, K.; Mailly, D. High resolution magnetic imaging: MicroSQUID Force Microscopy. *J. Phys. Conf. Ser.* **2008**, *97*, 012330. [CrossRef]
24. Skocpol, W.J.; Beasley, M.R.; Tinkham, M. Self-heating hotspots in superconducting thin-film microbridges. *J. Appl. Phys.* **1974**, *45*, 4054–4066. [CrossRef]
25. Wang, Z.; Nair, H.P.; Correa, G.C.; Jeong, J.; Lee, K.; Kim, E.S.; Lee, C.S.; Lim, H.J.; Muller, D.A.; Schlom, D.G. Epitaxial integration and properties of SrRuO$_3$ on silicon. *APL Mater.* **2018**, *6*, 086101. [CrossRef]
26. Sauer, B.; Gottfried-Gottfried, R.; Haase, T.; Kück, H. CMOS-compatible integration of thin ferromagnetic films. *Sens. Actuators A Phys.* **1994**, *42*, 582–584. [CrossRef]
27. Lloyd, J.C.; Smith, R.S. Structural and Magnetic Properties of Permalloy Films. *J. Appl. Phys.* **1959**, *30*, s274–s275. [CrossRef]
28. Arnold, H.D.; Elmen, G.W. Permalloy, an alloy of remarkable magnetic properties. *J. Frankl. Inst.* **1923**, *195*, 621–632. [CrossRef]
29. Park, H.J.; Ra, H.-W.; Song, K.S.; Hahn, Y.-B. Inductively Coupled Plasma Etching of Ta, Co, Fe, NiFe, NiFeCo, and MnNi with Cl$_2$/Ar Discharges. *Korean J. Chem. Eng.* **2004**, *21*, 1235–1239. [CrossRef]
30. Bryan, M.T.; Atkinson, D.; Cowburn, R.P. Edge roughness and coercivity in magnetic nanostructures. *J. Phys. Conf. Ser.* **2005**, *17*, 40–44. [CrossRef]
31. Available online: https://en.wikipedia.org/wiki/Stencil_lithography (accessed on 30 April 2023).
32. Tsioutsiosa, I.; Serniak, K.; Diamond, S.; Sivak, V.V.; Wang, Z.; Shankar, S.; Frunzio, L.; Schoelkopf, R.J.; Devoret, M.H. Free-standing silicon shadow masks for transmon qubit fabrication. *AIP Adv.* **2020**, *10*, 065120. [CrossRef]
33. Köhler, J.M.; Albrecht, M.; Musil, C.R.; Bucher, E. Direct growth of nanostructures by deposition through an Si$_3$N$_4$ shadow mask. *Phys. E Low-Dimens. Syst. Nanostruct.* **1999**, *4*, 196–200. [CrossRef]
34. Bates, J.R.; Miyahara, Y.; Burgess, J.A.J.; Iglesias-Freire, Ó.; Grutter, P. Effect of using stencil masks made by focused ion beam milling on permalloy (Ni$_{81}$Fe$_{19}$) nanostructures. *Nanotechnology* **2013**, *24*, 115301. [CrossRef]